Article:
Grobbe, N. and de Ridder, S.A.L. orcid.org/0000-0002-0797-7442 (2021) Seismoelectric surface-wave analysis for characterization of formation properties, using dispersive relative spectral amplitudes. Geophysics, 86 (3). A27-A31. ISSN 0016-8033

https://doi.org/10.1190/geo2020-0299.1

Seismoelectric Surface Wave Analysis for Characterization of Formation Properties, using Dispersive Relative Spectral Amplitudes

(November 20, 2020)

Running head: **Seismoelectric Surface Wave DRSA**

ABSTRACT

We study seismoelectric (SE) surface wave signals and find that they can be used to infer changes in the SE coupling properties at depth. Seismoelectric surface wave signals have much higher amplitudes than seismoelectric body wave signals. We propose to measure both the seismic and the electrical potential or electromagnetic (EM) field along the surface of the Earth. We use Dispersive Relative Spectral Amplitudes (DRSA) that measure the frequency dependent relative strength of electrical signals versus seismic signals associated with seismoelectric surface wave signals. We show that the DRSA have sensitivity to contrasts in the electrokinetic coupling coefficient and other relevant petrophysical properties at depth. Our discovery can mitigate the major limitation that plagues body wave-based SE methods: the relative weakness of the converted, EM signals from seismic body waves. We envision applications to characterize subsurface rock, fluid and fluid flow properties (e.g. porosity, permeability, and dynamic fluid viscosity, salinity) in the near-surface, for aquifers, and shallow geothermal reservoirs.

INTRODUCTION

Seismoelectric (SE) methods aim to provide information about, e.g.: rock formation porosity and permeability, pore-fluid properties such as the dynamic viscosity and salinity (Revil et al., 2015;

Butler et al., 2018), and fine-scale (thin-bedded) structural features (Grobbe and Slob, 2016).

Traditionally, SE methods focus on measuring electric fields generated by seismic body waves (Pride, 1994; Garambois and Dietrich, 2002) and suffer from the weak body wave interface response signal strengths. A variety of methodologies have been proposed, e.g. in terms of analysis (e.g., evanescent fields related to body-wave responses (Ren et al., 2016; Butler et al., 2018)), acquisition design (e.g. borehole surveys (Dupuis et al., 2009), SE vibroseis acquisition (Dean et al., 2012), and special electrode arrays (Dietrich et al., 2018)), seismoelectric focusing (Sava et al., 2014; El Koury et al., 2015; Grobbe et al., 2019), data processing (e.g., curvelets (Warden et al., 2012), spectral ratios applied to interface response signals (Dzieran et al., 2019)), and instrumentation design (preamplifier-electrode composites (Dupuis et al., 2007)), in attempts to utilize SE body wave signals; all with very limited success.

We focus for the first time on using SE surface waves. Surface waves are interface waves propagating along the free surface and can map subsurface seismic wave speeds (Bensen et al., 2008; De Ridder and Dellinger, 2011). Their sensitivity to subsurface heterogeneities and contrasts comes from oscillations at different frequencies that sense properties at different depths (Socco and Strobbia, 2004). SE surface waves have been successfully observed in the laboratory (Xiong et al., 2017) and in the field (Dupuis et al., 2007; Sun et al., 2019), but have not yet been considered for SE characterization. Surface waves show stronger amplitudes than body waves because their energy spreads in 2D (instead of in 3D) is concentrated near the Earth's surface. SE surface wave signals would yield medium properties at depth and aid studies of fluid processes in the Earth's crust.

SEISMOELECTRIC SURFACE WAVE SIGNALS

SE coupling phenomena originate in chemical reactions between the mineral surfaces and the pore fluids in the presence of potential-determining ions (Revil et al., 2015; Grobbe et al., 2020). Net charges arising at mineral surfaces are compensated by ions from the fluids in the so-called Stern and diffuse layers forming an electrical double layer (Stern, 1924; Revil et al., 2015). Mechanical disturbances causing fluid flow result in streaming potentials and SE coupling (Revil et al., 2015). The Pride-model (Pride, 1994), used here, may not adequately capture dispersive effects of microscopic origin (of e.g. electrical conductivity). To unambiguously attribute the observed macroscopic dispersive effects to surface wave physics, we avoid further complexity with microscopic dispersion effects. In practice, microscopic dispersive effects can occur and may pose an additional challenge.

We distinguish three types of SE coupling:

1. coseismic coupling: provides local information at the location of the seismic wave.
2. source-impact coupling: localized charge asymmetries generating a diffusing electromagnetic (EM) field which provides local subsurface information near the sources.
3. interface responses: at heterogeneities, asymmetries in the coseismic charge separation occur, creating a diffusive EM field; providing information from depth but with low signal strength.

Figure 1a shows an example of SE surface wave signals as observed in a vertical component electrical field due to a vertical dipole bulk force source (E_z^{fzb}), e.g. a weight drop. This gather was modeled for a single layer overlaying a halfspace using a highly precise analytic layered-Earth seismoelectric and electroseismic modeling code ESSEMOD (Grobbe, 2016). The layer thickness is 15 m, the Biot fast pressure wave (Pf) and shear wave (S) velocities for the $layer$ and halfspace (hs) are $c_{Pf;layer} = 2490.84$ m/s, $c_{S;layer} = 1336.32$ m/s and $c_{Pf;hs} = 3981.6$ m/s, $c_{S;hs} =$

1990.1 m/s. The source emits a Ricker wavelet ~~with peak frequency of 30 Hz~~ located at 0.5 m depth. 401 receivers measure both electrical fields and seismic particle velocity in a split spread array with a horizontal spacing of 10 m at 2.5 m depth (more detail: ancillary file).

[Figure 1 about here]

In Figure 1a, the strong, non-propagating signal at small offsets is a numerical artifact from the Fourier-Bessel transformations in ESSEMOD, discussed by Grobbe (2016) (we muted the small offsets and the source-converted EM field around t=0, before frequency-wavenumber (f-k) transformation. The strong cone of signals S_W reflects the dispersive nature of surface waves. The amplitudes of the SE surface wave signals are one to two orders of magnitude larger than SE signals from traditionally-considered wave types, i.e. the first arrival coseismic P-wave (P_d), refracted P wave (P_{rf}), and the source-converted EM field at $t = 0$ s (EM_d). In our conceptual model, seismoelectric surface waves convert to EM signals via two mechanisms: an effective coseismic component and an interface dipole component at subsurface contrasts (Figure 1b). The latter has similarities with evanescent EM waves predicted by Ren et al. (2016) and observed by Butler et al. (2018). The key difference is that for a P-wave that travels oblique along the interface, the particle motion is always incident on the interface at a post-critical angle, and the outgoing EM field is therefore evanescent. Whereas for a surface wave motion, the particle motion is elliptical and exhibits a full range of incidence angles on the interface. The outgoing EM field has a (classical) non-evanescent interface dipole component (generated when the ellipsoidal oscillatory motion is pre-critical to the interface) and an evanescent component (generated when particle wave motion is post critical to the interface).

MEASURING SEISMOELECTRIC SURFACE WAVE DISPERSIVE RELATIVE SPECTRAL AMPLITUDES

We define *Dispersive Relative Spectral Amplitudes* (DRSA) to analyze SE surface wave signals. This method extracts relative amplitude information (EM versus seismic) from dispersive SE surface wave signals as a function of frequency and removes the source signature. What remains is the dispersive nature of this DRSA for seismoelectric surface wave signals. In seismic and electric receiver gathers, v_z^{fzb} and E_z^{fzb}, we compute the f-k amplitude spectra to separate the wave types (Figure 2).

[Figure 2 about here]

The DRSA is computed as the ratio between the electric f-k and the seismic f-k spectra (breve indicates a quantity in the f-k domain):

$$D\breve{R}SA = \frac{\|\breve{E}_z^{fzb}\|}{(\|\breve{v}_z^{fzb})\| + \epsilon)}. \quad (1)$$

Analogously for other EM and seismic field components. For stability we added a small value ϵ to the denominator ($\epsilon = 0.00001 \cdot \max(\mathcal{R}(\breve{v}_z^{fzb}))$). We extract the values associated with the surface wave modes from the DRSA f-k data by tracing the peak of the surface wave energy. The DRSA requires both seismic and electrical observations. These could be measured simultaneously with an integrated recording system, or separately to avoid potential cross-talk (Dupuis et al., 2007).

DRSA FOR CHANGING COUPLING COEFFICIENTS

We consider a total of 9 models. The SE coupling coefficient in the lower halfspace is changed relative to the reference model (corresponding to Figures 1 and 2) and kept the same in the overlying layer (Table 1 and ancillary file).

[Table 1 about here]

The SE coupling coefficient (Pride, 1994) (i.e. the current coupling or dynamic electrokinetic coupling, not a voltage coupling, see Schoemaker et al. (2012)), which depends on petrophysical medium properties (e.g. porosity, dynamic viscosity, and zeta potential (Pride, 1994; Revil et al., 2015)), is changed by changing the electrolyte concentration of the pore-fluid (equations 2.8-2.18 in Grobbe (2016)) ~~only.~~ Consequently, the electrical conductivity of the halfspace changes as well. The changes in seismic velocity and density are insignificant and changes in the dispersive characteristics of the seismoelectric response as observed at the surface must originate from changes in the SE coupling and the electrical conductivity at depth. We take DRSA measurements for the fundamental mode surface wave signals for all simulations (shown in Figure 3a). The F-mode DRSA decreases with decreasing electrolyte concentration, or, in other words, as the coupling coefficient of the lower halfspace increases and the electrical conductivity decreases.

[Figure 3 about here]

We compute their difference with respect to the reference model (Figure 3b) and find that these increase as the contrast in seismoelectric coupling and electrical conductivity across the interface increases (albeit non-uniformly). At higher frequencies, the DRSA measurements from the different simulations converge.

DISCUSSION

Above 40 Hz the difference in DRSA measurements between different models is negligible. The wavelength of fundamental-mode Rayleigh waves reduces from 50 at 30 Hz to 37.5 m at 40 Hz (from phase velocity analysis) and the skin depth (approximately $1/3$ wavelength) reduces below

15 m, no longer sensing the half-space properties. The non-uniform distribution of the DRSA responses with the magnitude of the contrast indicates a complex relationship between SE DRSA measurements and the coupling coefficients and electrical conductivity, and their distribution. The DRSA sensitivity to changes in our models may be considered small, but increases for lower frequencies, or when changes occur at shallower depth. Moreover, the DRSA sensitivity of seismoelectric surface wave signals may be greater for other changes in petrophysical properties at depth. The interplay of changes in the contributions from the effective coseismic dipole and the interface response dipole result in a net amplitude change observed at the subsurface(conceptual diagram in Figure 1b). In our models, the interface response dipole is directed opposite to the field lines of the coseismic contributions and increasing coupling properties at depth can lead to a decreasing electrical field strength at the surface. We focused on Rayleigh-type fundamental-mode surface waves and analyzed the vertical component electric fields E_z and particle velocity fields v_z. E_z may be challenging to measure in the field. DRSAs can also be computed for Rayleigh and Love waves observed in the horizontal components. We anticipate that DRSA analysis of various SE surface wave modes would enable inference of different rock formation properties, with varying sensitivities, e.g. for different degrees of fluid saturation. The depth sensitivity of surface waves changes when the seismic properties of the medium change. Consequently, the excited dipole responses at depth change. The orientations of the dipoles are determined by the surface wave motion and the magnitude and polarity are determined by the poroelastic and coupling properties. The combination determines the precise changes in observable DRSAs. Surface waves in non-stratified media can be characterized with effective phase velocities (Wielandt, 1993); effective DRSAs could be used similarly.

CONCLUSIONS

Dispersive Relative Spectral Amplitudes (DRSA) of seismoelectric (SE) surface wave signals are sensitive to the SE coupling coefficient and other relevant petrophysical properties (e.g., electrical conductivity), at depth in the subsurface. Surface wave signals are the strongest of SE signals and have been observed in the field. Therefore, exploiting SE surface wave signals is a paradigm shift in SE data acquisition that may advance its integration in geophysical workflows and multi-scale applications across various geoscientific disciplines.

REFERENCES

Bensen, G. D., M. H. Ritzwoller, and N. M. Shapiro, 2008, Broadband ambient noise surface wave tomography across the United States: Journal of Geophysical Research: Solid Earth, **113**.

Butler, K. E., B. Kulessa, and A. J.-M. Pugin, 2018, Multimode seismoelectric phenomena generated using explosive and vibroseis sources: Geophysical Journal International, **213**, 836–850.

De Ridder, S., and J. Dellinger, 2011, Ambient seismic noise eikonal tomography for near-surface imaging at Valhall: The Leading Edge, **30**, 506–512.

Dean, T., C. Dupuis, R. Herrmann, and J. Valuri, 2012, A brute-strength approach to improving the quality of seismoelectric data: SEG Expanded Abstracts Las Vegas, 1–5.

Dietrich, M., M. S. Devi, S. Garambois, D. Brito, and C. Bordes, 2018, A novel approach for seismoelectric measurements using multielectrode arrangements – I: theory and numerical experiments: Geophysical Journal International, **215**, 61–80.

Dupuis, J. C., K. E. Butler, and A. W. Kepic, 2007, Seismoelectric imaging of the vadose zone of a sand aquifer: Geophysics, **72**, A81–A85.

Dupuis, J. C., K. E. Butler, A. W. Kepic, and B. D. Harris, 2009, Anatomy of a seismoelectric conversion: Measurements and conceptual modeling in boreholes penetrating a sandy aquifer: Journal of Geophysical Research: Solid Earth, **114**.

Dzieran, L., M. Thorwart, W. Rabbel, and O. Ritter, 2019, Quantifying interface responses with seismoelectric spectral ratios: Geophysical Journal International, **217**, 108–121.

El Koury, P., P. Sava, and A. Revil, 2015, Seismoelectric beamforming imaging: a sensitivity analysis: Geophysical Journal International, **201(3)**, 1781–1800.

Garambois, S., and M. Dietrich, 2002, Full waveform numerical simulations of seismoelectromagnetic wave conversions in fluid-saturated stratified porous media: Journal of Geophysical Research, **107-B7**, 11–12.

Grobbe, N., 2016, Coupled poroelastic waves and electromagnetic fields in layered media: theory, modeling, and interferometric synthesis: Ph.D. Dissertation, Delft University of Technology, ~~1–342.~~

Grobbe, N., A. Fournier, and L. Demanet, 2019, Systems and methods for detecting seismo-electromagnetic conversion: U.S. Patent Application Publication, **US2019/0293832A1**, ~~p.~~1–20.

Grobbe, N., A. Revil, Z. Zhu, and E. Slob, 2020, Seismoelectric exploration: Theory, experiments, and applications, ISBN: ~~978-1-119-12737-6.~~ John Wiley & Sons, Ltd.

Grobbe, N., and E. Slob, 2016, Seismo-electromagnetic thin-bed responses: Natural signal enhancements?: Journal of Geophysical Research - Solid Earth, **121**, 2460–2479.

Pride, S., 1994, Governing equations for the coupled electromagnetics and acoustics of porous media: Physical Review B., **50-21**, 15678–15696.

Ren, H., Q. Huang, and X. Chen, 2016, Existence of evanescent electromagnetic waves resulting from seismoelectric conversion at a solid–porous interface: Geophysical Journal International, **204**, 147–166.

Revil, A., A. Jardani, P. Sava, and A. Haas, 2015, The seismoelectric method: Theory and application: John Wiley & Sons, Ltd.

Sava, P., A. Revil, and M. Karaoulis, 2014, Cross-well electrical resistivity imaging using seismoelectric focusing and image-guided inversion: Geophysical Journal International, **198**, 880–894.

Schoemaker, F., N. Grobbe, M. Schakel, S. de Ridder, E. Slob, and D. Smeulders, 2012, Experimental validation of the electrokinetic theory and development of seismoelectric interferometry by cross-correlation: International Journal of Geophysics, **2012**.

Socco, L., and C. Strobbia, 2004, Surface-wave method for near-surface characterization: a tutorial: Near Surface Geophysics, **2**, 165–185.

Stern, O., 1924, The theory of the electrolytic double-layer: Elektro-chemistry, **30**, 508.

Sun, Y.-C., M. Uyeshima, H. Ren, Q. Huang, K. Aizawa, K. Tsukamoto, W. Kanda, K. Seki, T. Kishita, T. Ohminato, A. Watanabe, and J. Ran, 2019, Numerical simulations to explain the coseismic electromagnetic signals: a case study for a m5.4 aftershock of the 2016 ~~kumamoto~~ earthquake: Earth, Planets and Space, **71**, 1–24.

Warden, S., S. Garambois, P. Sailhac, L. Jouniaux, and M. Bano, 2012, Curvelet-based seismoelectric data processing: Geophysical Journal International, **190**, 1533–1550.

Wielandt, E., 1993, Propagation and structural interpretation of non-plane waves: Geophysical Journal International, **113**, 45–53.

Xiong, Z., Z. Liu, and K. Zhang, 2017, An experimental study of Rayleigh waves based on seismoelectric measurements: Exploration Geophysics, **48**, 226–236.

FIGURES AND TABLES

Model	$\hat{\mathcal{L}}_{layer}$	$\hat{\mathcal{L}}_{hs}$	c_{layer} [mol/L]	c_{hs} [mol/L]	σ^e_{layer} [sm^{-1}]	σ^e_{hs} [Sm^{-1}]
Model 1	$1.15{\cdot}10^{-8}$	$4.15{\cdot}10^{-9}$	$1.0\cdot10^{-5}$	$1.0{\cdot}10^{-2}$	$1.24\cdot10^{-4}$	0.12
Model 2	$1.15{\cdot}10^{-8}$	$6.61{\cdot}10^{-9}$	$1.0\cdot10^{-5}$	$1.0{\cdot}10^{-3}$	$1.24\cdot10^{-4}$	$1.24\cdot10^{-2}$
Model 3	$1.15{\cdot}10^{-8}$	$7.35{\cdot}10^{-9}$	$1.0\cdot10^{-5}$	$5.0{\cdot}10^{-4}$	$1.24\cdot10^{-4}$	$6.18\cdot10^{-3}$
Model 4	$1.15{\cdot}10^{-8}$	$9.06{\cdot}10^{-9}$	$1.0\cdot10^{-5}$	$1.0{\cdot}10^{-4}$	$1.24\cdot10^{-4}$	$1.24\cdot10^{-3}$
Model 5	$1.15{\cdot}10^{-8}$	$9.79{\cdot}10^{-9}$	$1.0\cdot10^{-5}$	$5.0{\cdot}10^{-5}$	$1.24\cdot10^{-4}$	$6.18\cdot10^{-4}$
Reference Model	$1.15{\cdot}10^{-8}$	$1.15{\cdot}10^{-8}$	$1.0\cdot10^{-5}$	$1.0{\cdot}10^{-5}$	$1.24\cdot10^{-4}$	$1.24\cdot10^{-4}$
Model 6	$1.15{\cdot}10^{-8}$	$1.22{\cdot}10^{-8}$	$1.0\cdot10^{-5}$	$5.0{\cdot}10^{-6}$	$1.24\cdot10^{-4}$	$6.18\cdot10^{-5}$
Model 7	$1.15{\cdot}10^{-8}$	$1.38{\cdot}10^{-8}$	$1.0\cdot10^{-5}$	$1.0{\cdot}10^{-6}$	$1.24\cdot10^{-4}$	$1.24\cdot10^{-5}$
Model 8	$1.15{\cdot}10^{-8}$	$1.58{\cdot}10^{-8}$	$1.0\cdot10^{-5}$	$1.0{\cdot}10^{-7}$	$1.24\cdot10^{-4}$	$1.24\cdot10^{-6}$

Table 1: Overview of the SE coupling coefficients $\hat{\mathcal{L}}$ in [$m^2\cdot s^{-1}\cdot V^{-1}$], electrolyte concentration, and electrical conductivity for both the layer and the halfspace, for the 9 different synthetic models. The colors correspond to the line colors in Figure 3. The reference model is displayed in red. These parameters are the only properties that vary between the models, the remainder of all modeling parameters are specified in an ancillary file.

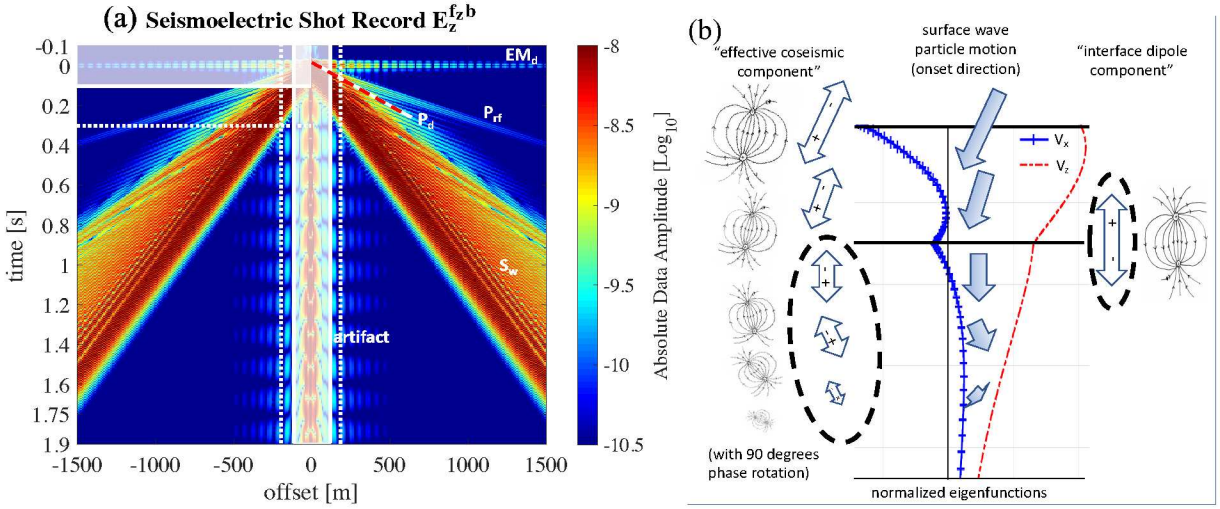

Figure 1: a) Seismoelectric shot record: a vertical component electrical field due to a vertical dipole bulk force source (E_z^{fzb} [Vm^{-1}]). Solid and dashed lines indicate the lower and upper ends of the applied Hanning taper (mute), respectively (for clarity only drawn for negative offsets). b) Conceptual diagram showcasing the different contributions to the SE surface wave signal; an effective coseismic component and an interface dipole-contribution. Arrows indicate the direction of onset of the particle velocity (as determined by the eigenfunctions of the fundamental mode Rayleigh waves at 30 Hz (blue and red curves) for the model of Table 1) and the associated electric dipoles in the coseismic and interface contributions. The surface wave eigenfunctions and the coseismic dipoles become weaker with depth. The black-dashed lines indicate the dipole contributions that change when the coupling properties below the interface change. Surface waves excite the medium from the free surface down to the depth of zero-displacement and all SE conversions occur simultaneously forming an 'effective coseismic dipole'. The characteristics of the interface dipole will depend on all contrasts in medium properties. For our models, the coseismic and interface contributions have opposite orientation. Both contributions occur practically simultaneously and with a 90-degree phase rotation. Their combination causes a net SE surface wave amplitude.

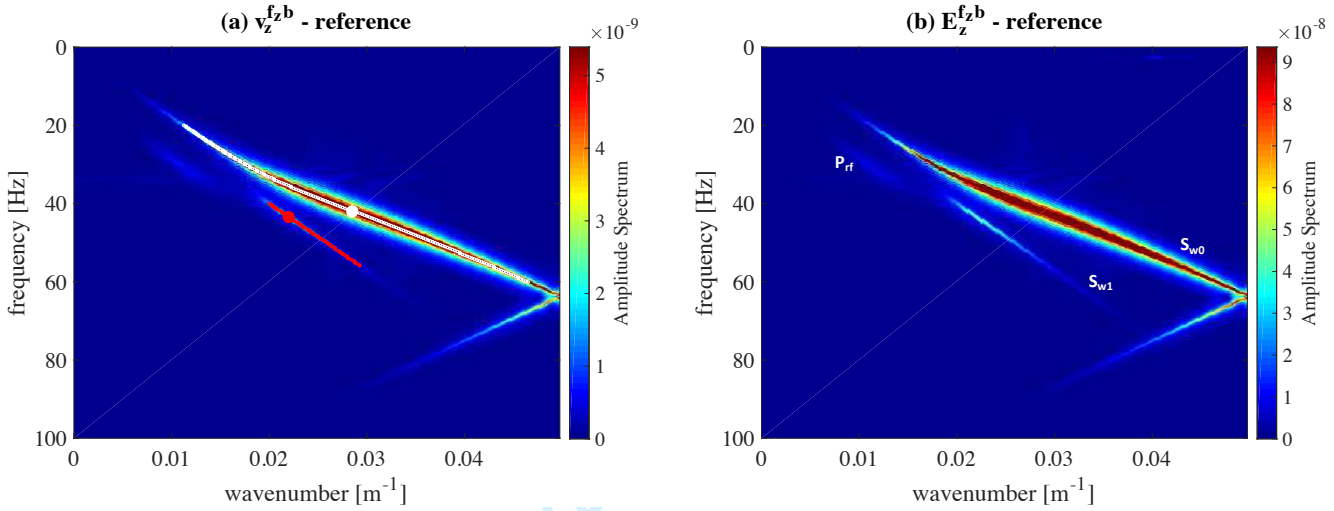

Figure 2: Frequency-wavenumber spectra for the reference model for (a) v_z^{fzb} [m] and (b) E_z^{fzb} [V m^{-1}] observations (having muted the Fourier-Bessel artifact and the source-converted EM field). The fundamental and first surface wave modes are annotated as S_{w0} and S_{w1} and the refracted energy as P_{rf}. The picked (f,k) values for the fundamental (in white) and first overtone (in red) surface wave modes are denoted by dotted lines; the larger dot is the initial pick input data point to our auto-picker. The units of the amplitude spectra for v_z^{fzb} and E_z^{fzb} are [m s s^{-1}= m] and [V s m^{-1}], respectively.

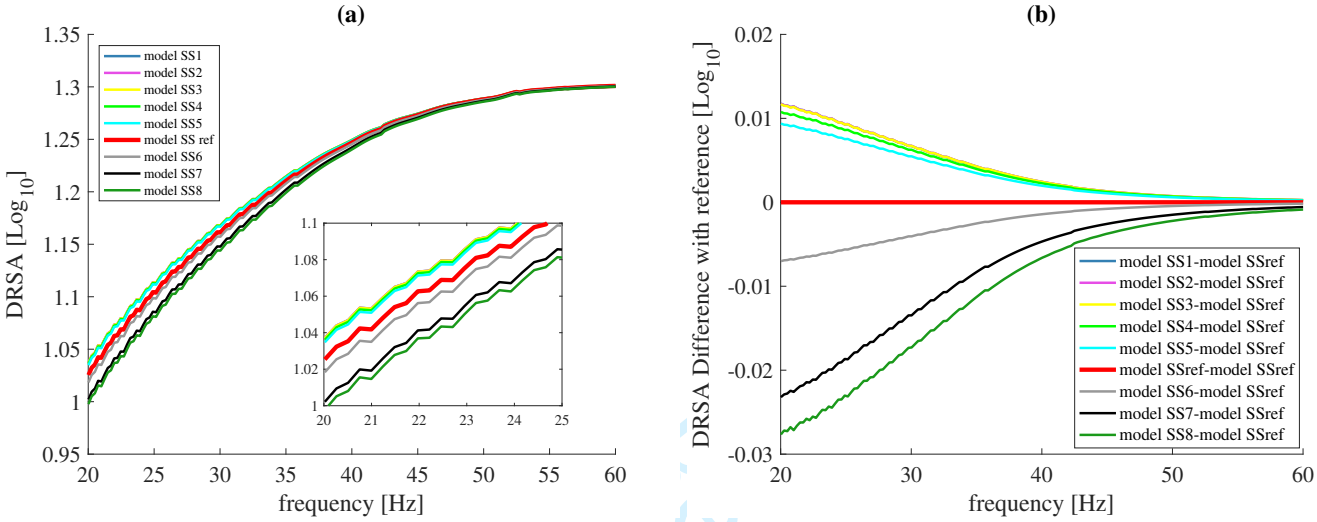

Figure 3: a) Fundamental mode seismoelectric surface wave dispersive relative spectral amplitude measurements [V s m^{-2}]. b) Difference in DRSA measurements with respect to the reference model.